MIT Open Access Articles

Multimodal spectroscopy detects features of vulnerable atherosclerotic plaque

Massachusetts Institute of Technology

Multimodal spectroscopy detects features of vulnerable atherosclerotic plaque

Obrad R. Šćepanović,ᵃ Maryann Fitzmaurice,ᵇ Arnold Miller,ᶜ Chae-Ryon Kong,ᵃ Zoya Volynskaya,ᵃ Ramachandra R. Dasari,ᵃ John R. Kramer,ᵃ and Michael S. Feldᵃ
ᵃMassachusetts Institute of Technology, George R. Harrison Spectroscopy Laboratory, Cambridge, Massachusetts 02139
ᵇCase Western Reserve University, Department of Pathology, Cleveland, Ohio 44106
ᶜMetroWest Medical Center, Department of Vascular Surgery, Natick, Massachusetts 01760

Abstract. Early detection and treatment of rupture-prone vulnerable atherosclerotic plaques is critical to reducing patient mortality associated with cardiovascular disease. The combination of reflectance, fluorescence, and Raman spectroscopy—termed multimodal spectroscopy (MMS)—provides detailed biochemical information about tissue and can detect vulnerable plaque features: thin fibrous cap (TFC), necrotic core (NC), superficial foam cells (SFC), and thrombus. *Ex vivo* MMS spectra are collected from 12 patients that underwent carotid endarterectomy or femoral bypass surgery. Data are collected by means of a unitary MMS optical fiber probe and a portable clinical instrument. Blinded histopathological analysis is used to assess the vulnerability of each spectrally evaluated artery lesion. Modeling of the *ex vivo* MMS spectra produce objective parameters that correlate with the presence of vulnerable plaque features: TFC with fluorescence parameters indicative of collagen presence; NC/SFC with a combination of diffuse reflectance β-carotene/ceroid absorption and the Raman spectral signature of lipids; and thrombus with its Raman signature. Using these parameters, suspected vulnerable plaques can be detected with a sensitivity of 96% and specificity of 72%. These encouraging results warrant the continued development of MMS as a catheter-based clinical diagnostic technique for early detection of vulnerable plaques. © *2011 Society of Photo-Optical Instrumentation Engineers (SPIE).* [DOI: 10.1117/1.3525287]

Keywords: atherosclerosis; vulnerable plaque; spectroscopy; Raman, fluorescence; reflectance; multimodal.

Paper 10173SSR received Apr. 1, 2010; revised manuscript received Aug. 23, 2010; accepted for publication Aug. 25, 2010; published online Jan. 20, 2011.

1 Introduction

Up to 70% of acute ischemic events result from the rupture of asymptomatic vulnerable atherosclerotic plaques, leading to thrombotic occlusion and myocardial infarction or stroke.[1,2] Most of these thrombosed plaques do not exhibit a clinically significant stenosis and are thus not routinely detected and treated.[1] The key features of vulnerable plaque include a thin fibrous cap (≤ 65 μm in thickness) and a large (>2 mm in diameter) necrotic core or superficial foam cells.[1–3] Other common features associated with plaque vulnerability are thrombus and acute intraplaque hemorrhage (or dissection), as they are commonly found in ruptured/thrombotic plaques.[1,2,4] These vulnerable plaques, if not completely occlusive, still pose a threat to the patient in the form of a subsequent rupture leading to an occlusive and lethal thrombosis.[3]

A number of imaging techniques are being developed for detecting vulnerable plaque, including intravascular ultrasound, magnetic resonance imaging, optical coherence tomography, and thermography.[5] These techniques detect changes in tissue density, refractive index, or temperature as an indication of vulnerability. Spectroscopic techniques are also being studied, with advances in fluorescence spectroscopy,[6,7] near-infrared spectroscopy,[8] and Raman spectroscopy.[9] The advantage of the spectroscopic techniques is that they provide biochemical

and morphological information about artery tissue composition that is most likely not obtained with nonspectroscopic techniques.[5]

With the development of the Raman probe[10] and clinical Raman instrument,[11] our laboratory was the first to demonstrate the potential of Raman spectroscopy to assess atherosclerotic plaque *in vivo*.[9] Independently, we have also shown the potential of diffuse reflectance spectroscopy (DRS) and intrinsic fluorescence spectroscopy (IFS) to detect plaque vulnerability features such as superficial foam cells.[12] By combining DRS, IFS, and Raman spectroscopy, a methodology we call multimodal spectroscopy (MMS), we can obtain even more detailed information about the disease state of the plaque.[13] The spectroscopic information provided by the three components of MMS is complementary and depth sensitive. The absorption and scattering properties of tissue are assessed by DRS, which provides information about hemoglobin and β-carotene/ceroid. IFS measures tissue fluorophores such as collagen, elastin, and lipids, while Raman spectroscopy provides molecule-specific information that can be used to identify a broad range of morphological features, including calcifications and lipid pools. Moreover, since the wavelength of light used for DRS, IFS, and Raman spectroscopy spans the 300- to 1000-nm range, over which light penetration in tissue varies significantly, the MMS technique provides a tool for sensing depth; specifically, light returning at shorter wavelengths will assess more superficial tissue properties than light returning at longer wavelengths.

Address all correspondence to: Obrad R. Šćepanović, Massachusetts Institute of Technology, G. R. Harrison Spectroscopy Laboratory, 77 Massachusetts Avenue, Room 6-205, Cambridge, MA 02139. Tel: (617) 680-6576; Fax: (617) 253-4513; E-mail: obrad@alum.mit.edu.

We have previously shown the potential for MMS to detect vulnerable plaques in an *in vitro* pilot study of carotid artery specimens.[13]

The present study is, to our knowledge, the first to date that aims to demonstrate the clinical feasibility of MMS for diagnostic application in human patients. More specifically, our goal is to show that MMS can accurately detect vulnerable or thrombotic plaques, enabling clinicians to identify a potentially lethal pathology before it becomes clinically evident.

2 Methods

Spectroscopic analysis of human artery tissue with MMS was performed both *in vivo* and *ex vivo*. Detailed histological analysis from the tissue sites was used to corroborate the spectroscopic findings. As the histology could be accurately aligned only with the *ex vivo* data, all results in this work are based on the *ex vivo* dataset. (Nevertheless, the method of collection of the *in vivo* data is also described, the purpose being to motivate future clinical feasibility of the MMS.) Based on the results, a preliminary diagnostic algorithm for detecting vulnerable plaques was developed.

2.1 Patient Population

Twelve patients participated in this study, eight men and four women, average age 72 years (range 53 to 90 years). Eight patients underwent carotid endarterectomy, three for a clinical history of stroke or transient ischemic attack, and five for an asymptomatic critical carotid artery stenosis. The remaining four patients underwent femoral bypass surgery for symptomatic peripheral artery disease. The MetroWest Medical Center and University Hospitals, Case Medical Center Institutional Review Boards and the MIT Committee of the Use of Humans as Experimental Subjects approved this study.

2.2 Clinical Multimodal Spectroscopy System

Data were collected with an integrated clinical MMS instrument and spectral probe developed in our laboratory. For a full description of the system, please refer to the related publication.[14] In brief, the MMS instrument utilized a xenon flash lamp (370 to 740 nm) to obtain reflectance spectra, a nitrogen laser (337 nm) to excite fluorescence, and a diode laser (830 nm) for Raman scattering. MMS spectra were collected by means of a *unitary* spectral probe previously sterilized overnight by either cold gas ethylene oxide or Sterrad® (Advanced Sterilization Products, Irvine, California). The probe contained a single excitation fiber and a concentric ring of 15 collection fibers, 10 of which were used to collect Raman spectra, and the remaining five to collect reflectance and fluorescence. The probe tip contained a ball lens to optimize signal collection as well as special filters that enable the collection of the relatively weak Raman signals.[10] The collected MMS spectra were dispersed by a spectrograph and recorded with a charge-coupled device (CCD) detector. The operation of the system was fully automated and controlled by an integrated software interface. Before data collection, calibration spectra were loaded onto the computer for real-time display of the acquired spectra and the ensuing data analysis.

2.3 Spectral Calibration

MMS calibration spectra were obtained prior to experimental data collection, as described previously.[13] These calibration spectra included: 4-acetamidophenol for Raman wave number calibration; an aluminum surface for Raman probe background; white light scattered off $BaSO_4$ for Raman spectral correction; a mercury lamp for DRS/IFS wavelength calibration; a 20% Spectralon reflectance standard for DRS intensity calibration; and deionized water in an opaque cup for DRS and IFS background characterization.

2.4 In Vivo Spectral Collection

MMS data were collected *in vivo* during femoral bypass and carotid endarterectomy surgeries performed at MetroWest between October 2007 and February 2008. During each surgery, the MMS instrument was wheeled into the operating room shortly after the start of the surgery and placed within a few feet of the patient, just outside the sterile field. The 4-m-long MMS probe, which had been previously sterilized overnight by either cold gas ethylene oxide or Sterrad®, was connected to the MMS instrument while keeping the proximal end in the sterile field. The instrument was turned on and software activated for data acquisition. Calibration spectra were loaded onto the computer for real-time display of the acquired spectra and the ensuing data analysis. Spectra collected *in vivo* typically consisted of a 2.5-s 830-nm exposure for Raman spectroscopy (10 consecutive exposures of 0.25 s each), ~1-s flashlamp exposure for DRS (five to seven pulses of light, 3 μs/pulse, ~7-Hz repetition rate), and ~1-s N_2 laser exposure for IFS (five to seven pulses of light, 3.5 ns/pulse, ~7-Hz repetition rate), resulting in a total exposure time per tissue site of less than 5 s. The excitation powers for the three modalities were typically: 100 mW from the 830-nm diode laser for Raman spectroscopy, ~2 μJ per flashlamp pulse of measured at 575 nm for DRS, and ~4 μJ per pulse of the N_2 laser measured at 337 nm for IFS. The operating room and surgical lights were turned off during data collection.

During a femoral bypass procedure, a stenotic or occluded portion of one of the arteries in the lower limbs (usually the femoral artery) is bypassed by a synthetic graft that restores adequate blood flow beyond the blocked portion of the vessel. For these studies, the surgeon inserted the front-viewing MMS probe through the proximal anastomosis site to make direct perpendicular contact with the posterior wall of the saline-flushed artery. Spectra were also collected adjacent to the incision on the intimal side of the artery, where the graft would later be attached. A biopsy was taken from this site and kept in saline for later spectroscopic examination *ex vivo*.

During a carotid endarterectomy, a severe accumulation of plaque lining the interior of the carotid artery, typically near a bifurcation, is directly removed, after which the artery wall is restored with a synthetic patch. For these studies, the diseased portion of the artery was clamped off on both sides with a shunt inserted to maintain blood flow to that half of the brain, and incised along the artery to expose the occlusive plaque. Spectra were then collected from the intimal surface of the saline-flushed plaque with the probe perpendicular to the artery wall,

and plaque was surgically removed and kept in saline for later spectroscopic data collection *ex vivo*.

In total, *in vivo* MMS spectra were collected at 40 locations from 9 of 12 patients.

2.5 Ex Vivo Spectral Collection

Ex vivo studies were also performed on the excised artery specimens within one hour of surgical excision. Spectra were collected *ex vivo* from multiple locations on the excised specimen, covering those areas spectrally examined *in vivo*, as well as other locations not examined *in vivo* owing to lack of time during surgery. The probe was held perpendicular to the artery and stabilized with a holding clamp. The room lights were turned off during spectral data acquisition. *Ex vivo* acquisition was typically done with exposures of 5 s for Raman spectra (20 exposures of 0.25 s each), ~1.5-s for DRS (ten pulses of light, 3 μs/pulse, ~7-Hz repetition rate), and ~1.5-s for IFS (ten pulses of light, 3.5 ns/pulse, ~7-Hz repetition rate); *ex vivo* exposures were purposely longer than those used *in vivo* to increase the signal-to-noise ratio of each measurement, while the excitation powers for the three modalities were approximately the same as those used *in vivo*. The excitation energy of the N_2 laser impinging on the tissue (μJ/pulse) measured each day was recorded so that the IFS spectra could be appropriately normalized later.

In total, *ex vivo* MMS spectra were collected at 84 locations from 11 of 12 patients.

Following *ex vivo* spectral data acquisition, the tissue evaluation site was demarcated with colloidal ink, and the specimen fixed in formalin and submitted for histological analysis. The location marked with colloidal ink served to register the *ex vivo* spectral evaluation site to the corresponding histology.

2.6 Spectral Data Analysis

The MMS spectra were processed and analyzed according to procedures described previously.[13] A summary of the modeling components and the fits of representative observed spectra are given in Fig. 1.

2.6.1 Diffuse reflectance

Briefly, the DRS spectra were calibrated by removing the background from the raw reflectance and dividing by the response of the Spectralon reflectance standard with known reflectivity. The diffusion theory model of Farrell, Patterson, and Wilson[15] was then fit to the calibrated DRS spectra using a standard error minimization technique to extract the reduced scattering coefficient $\mu'_s(\lambda)$ and the absorption coefficient $\mu_a(\lambda)$, which were modeled as:

$$\mu'_s(\lambda) = A \cdot (\lambda/\lambda_0)^{-B}, \tag{1}$$

$$\mu_a(\lambda) = C_{\text{diff}}(\lambda)v\big[\alpha \cdot \varepsilon_{\text{HbO}_2}(\lambda) + (1-\alpha) \cdot \varepsilon_{\text{Hb}}(\lambda)\big]$$
$$+ c_{\beta-\text{car}}\varepsilon_{\beta-\text{car}}(\lambda) + c_{\text{ceroid}}\varepsilon_{\text{ceroid}}(\lambda), \tag{2}$$

where $\lambda_o = 1$ μm, and the parameters A and B specified the power law dependence, as justified elsewhere.[16,17] The dominant artery tissue absorbers in the visible wavelength range

are hemoglobin, β-carotene, and ceroid, and the quantities employed to model them, $\varepsilon_{\text{HbO}_2}(\lambda)$, $\varepsilon_{\text{Hb}}(\lambda)$, $\varepsilon_{\beta-\text{car}}(\lambda)$, and $\varepsilon_{\text{ceroid}}(\lambda)$ were the extinction coefficients of oxyhemoglobin, deoxyhemoglobin, β-carotene, and ceroid,[18] respectively, with α being the hemoglobin saturation parameter. The parameter v was the blood volume fraction, $v = c_{\text{Hb}}/(150$ mg/ml), and the parameter $C_{\text{diff}}(\lambda)$ was used to account for the inhomogeneous distribution of hemoglobin in blood vessels.[19]

The extinction coefficients of the tissue absorbers at unit concentrations are shown in Fig. 1(a). The experimental data were fit to the model [Fig. 1(b)] using a standard optimization method that minimized the difference between the DRS data spectrum and fit in the range from 370 to 740 nm. The fits resulted in an estimate of the $\mu'_s(\lambda)$ and $\mu_a(\lambda)$ values of the tissue, which are characterized by parameters $A, B, c_{\text{Hb}}, \alpha, c_{\beta-\text{car}}$, c_{ceroid}, and C_{diff}.

2.6.2 Intrinsic fluorescence

The IFS spectra were extracted by subtracting the background from the raw fluorescence and applying the IFS correction procedure of Zhang et al.,[20] which uses the DRS spectrum to correct for distortions of the fluorescence spectrum due to tissue scattering and absorption. Then, as done previously,[13] the IFS spectra were used to develop an IFS model using multivariate curve resolution (MCR). The spectral features of the IFS signals could be well characterized using two MCR components, one collagen-like and another elastin/lipid-like, both shown in Fig. 1(c). The IFS spectra were fit in the range 370 to 640 nm using these two MCR components [Fig. 1(d)], with ordinary least squares to yield the contributions of each. The extracted collagen-like (C_{337}) and elastin/lipid-like (E_{337}) coefficient indicated the contributions of collagen- and elastin/lipid-like constituent spectra to the observed spectra.

2.6.3 Raman spectroscopy

The Raman spectra were extracted after background subtraction, spectral response correction, and removal of tissue fluorescence using a sixth-order polynomial.[10] The Raman spectra, normalized to peak height, were then fit using ordinary least squares to the linear combination model of Buschman et al.[21] to yield the contributions of the Raman active components of the artery wall ("fit coefficients"). The relevant morphological basis spectra included cholesterol crystals (CC), calcium mineralization (CM), foam cells / necrotic core (FC/NC), and thrombus. (Note that currently Raman spectroscopy cannot differentiate the spectral contribution of foam cells from that of necrotic core.) In the course of the study, we also collected spectra from a large (>2 mm thick) thrombus that was excised from the lumen of an artery. The Raman spectrum from this thrombus was also used as a morphological basis spectrum to model the presence of a thrombus in other samples, and was thus added to the constituent spectral library of Buschman et al.[21] The Raman basis spectra of all the morphological structures are given in Fig. 1(e). The sum of the contributions for each lesion was normalized to unity; in this way, the fit coefficients provide a relative contribution of each tissue constituent. A representative Raman spectrum and corresponding fit is given in Fig. 1(f).
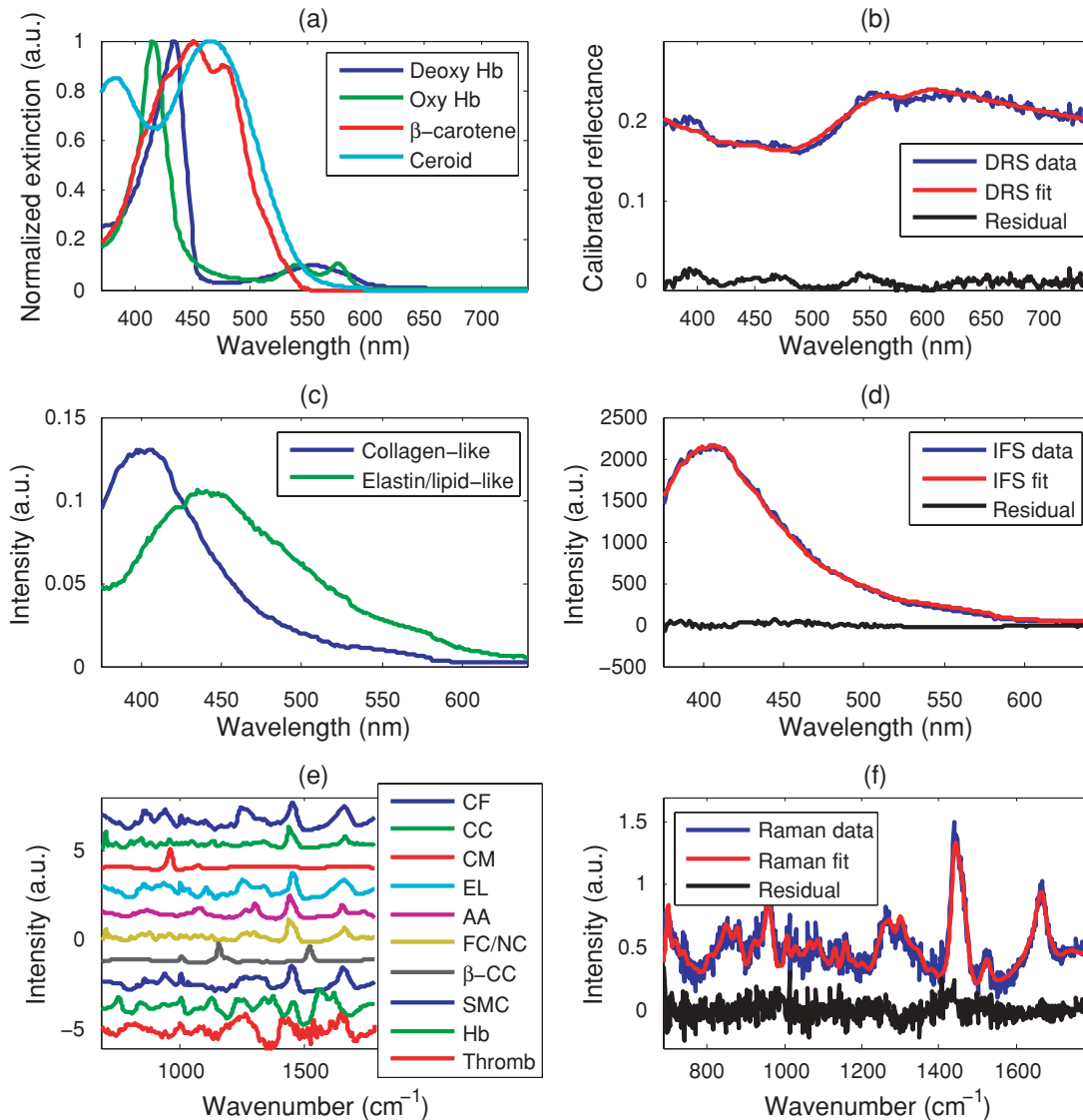
Fig. 1 (a) Absorption coefficients used to model the tissue absorbers for DRS modeling; (b) representative experimental data and fit for DRS; (c) basis spectra, obtained through MCR, used to model IFS spectra; (d) representative experimental data and fit for IFS; (e) Raman morphological basis spectra, including thrombus; and (f) representative experimental data and fit for a representative Raman spectrum. The representative spectra in (b), (d), and (f) are collected *ex vivo* from the same tissue location, a carotid artery calcified atheromatous plaque.

In summary, the relevant extracted DRS spectral parameters $c_{\beta-\mathrm{car}}$ and c_{ceroid} specified the contributions of the tissue absorbers β-carotene and ceroid, respectively. The relevant extracted IRS parameters C_{337} and E_{337} indicated the contributions of collagen- and elastin/lipid-like constituent spectra, respectively. The relevant extracted Raman spectroscopy parameters included the contributions of CC, contributions of FC/NC, and that of thrombus.

2.7 *Histological Analysis*

The demarcated tissue specimens were routinely processed, sectioned, and stained with hematoxylin and eosin. Histopathology for each of the specimens was then performed by an experienced cardiovascular pathologist blinded to the spectroscopy results. Each spectral location was diagnosed using the SNOMED classification system[22] as nonplaque (intimal fibroplasia) or plaque (atherosclerotic, atheromatous, or fibrotic-sclerotic). A number of morphological features associated with plaque vulnerability were also assessed, examples of which are presented in Fig. 2. Fibrous cap thickness was recorded as the range of thicknesses found underneath the ink dot [Figs. 2(a) and 2(b)]; the fibrous cap was also examined for the presence of rupture or ulceration [Fig. 2(d)]. Necrotic core size was recorded as the maximum dimension of the core beneath the fibrous cap [Fig. 2(b)]. The presence of foam cells was evaluated based on the most superficial depth at which they were found, along with a density grade ($0 =$ none; $1+ =$ isolated single foam cells; $2+ =$ small clusters of foam cells; and $3+ =$ confluent sheets of foam cells) [Fig. 2(c)]. The presence or absence of thrombus on the luminal surface of the artery was also noted [Fig. 2(d)], and the size of the thrombus was recorded as the maximum dimension underneath the ink dot.
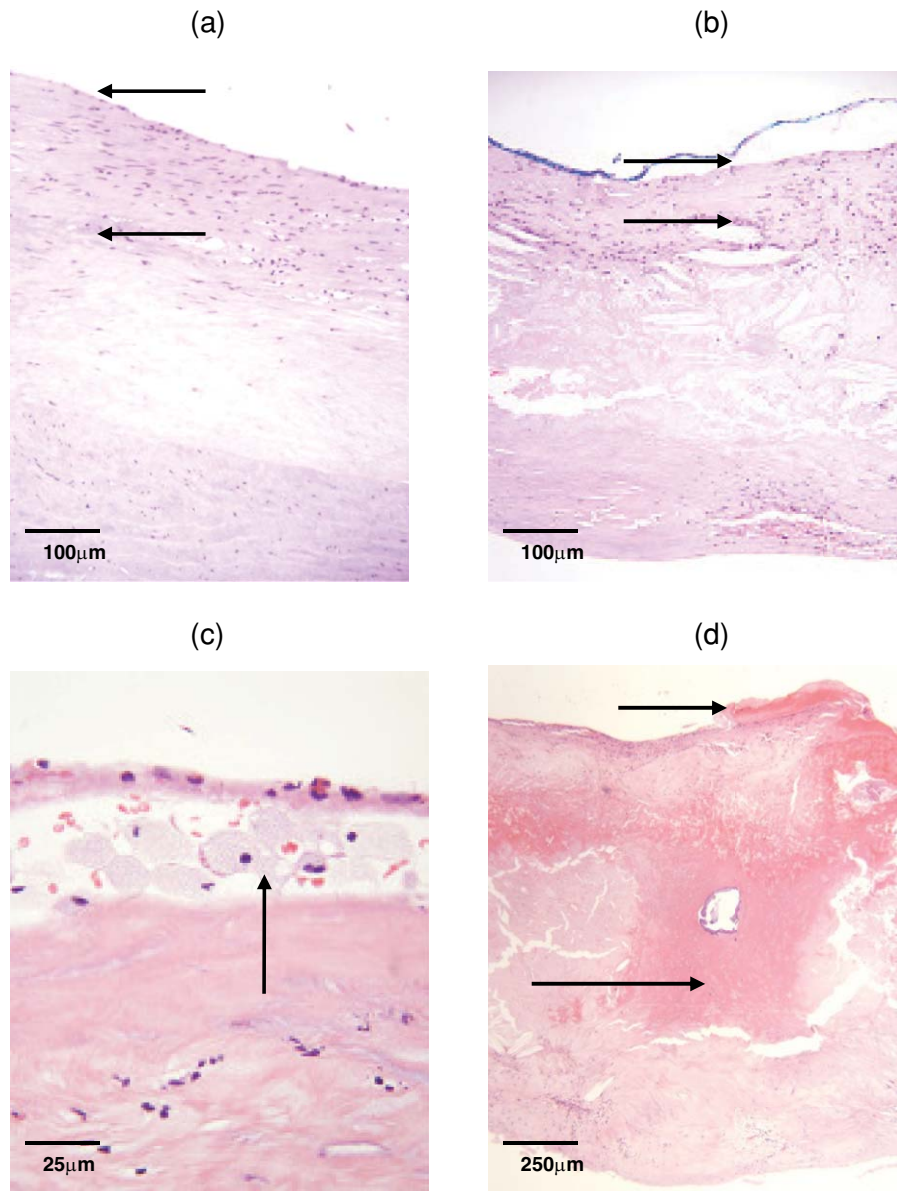
Fig. 2 Photomicrographs of representative tissue sites: (a) atherosclerotic plaque with thick fibrous cap (HE; 10×; intimal thickness 200 μm, indicated by arrows); (b) thin fibrous cap atheroma (HE; 10×; intimal thickness 65 μm, indicated by arrows); (c) superficial foam cells grade 3 + (HE; 40×; arrow); and (d) ulcerated thin fibrous cap atheroma, with thrombus (short arrow; thrombus thickness 70 μm) and acute intraplaque hemorrhage (long arrow) (HE; 4×).

2.8 Diagnosis and Classification

We developed a spectroscopic test (classifier) for this study to identify vulnerable plaques as assessed by the standard of histology, utilizing logistic regression and leave-one-out cross validation.[23] We evaluated the robustness of the classifiers using receiver operating characteristic (ROC) curves, as well as related metrics such as the sensitivity, specificity, positive predictive value (PPV), negative predictive value (NVP), and test efficiency (overall accuracy). The area under the ROC curve (compared to a maximum area of unity for a perfect classifier) indicates the robustness of the classifier more soundly than any particular single combination of sensitivity and specificity. Since the ROC curve specifies the possible trade-offs between

sensitivity and specificity for a family of related classifiers, one can to choose a particular classifier (associated with a particular operating point on the ROC curve) based on optimizing some test metric. In this work, we choose the classifier whose operating point results in maximal test efficiency.

3 Results

As indicated earlier, the following analysis and results are based on *ex vivo* data, as only for this spectral dataset could direct comparisons to histology be made. Owing to histological processing difficulties, two spectral locations were excluded from the study. In addition, six more spectral locations were excluded

Table 1 Plaque vulnerability criteria. The table summarizes how many spectral evaluation sites were determined to be in each category according to histology. Vulnerable plaques are defined as having both: (1) a thin (≤ 65 μm) fibrous cap, and (2) a large necrotic core (≥ 500 μm), or an accumulation of superficial foam cells (≤ 65 μm deep with a density of at least $3+$). These criteria resulted in a total of 23 vulnerable plaques; one plaque with a borderline thin fibrous cap (80 μm) was categorized as vulnerable by exception, as it had both a large necrotic core and an accumulation of superficial foam cells.

Morphologic feature	Criteria	Number of spectral locations
Thin fibrous cap	≤ 65 μm	22
	> 65 μm	54
Necrotic core	≥ 500 μm	36
	< 500 μm	40
Superficial foam cells	$3+$	5
	0 or $1+$ or $2+$	71
Thrombus	Present	13
	Absent	63
Total		76

because at least one of the MMS modalities contained excessive noise or incorrigible experimental artifacts. The remaining 76 (out of original 84) spectral locations examined *ex vivo* were used in the following analysis and exhibited a wide variety of morphological, structural, and pathological variations.

3.1 Histological Findings

Detailed morphological assessment was performed for every spectral site, as indicated in Table 1.

78% of spectral locations (59/76) were diagnosed as plaques. We defined *vulnerable plaques* as those lesions that exhibited both (1) a *thin* (≤ 65 μm) fibrous cap (TFC), and (2) a *large* (≥ 500 μm) necrotic core (NC) or an *accumulation* of superficial foam cells (SFCs) (≤ 65 μm deep with a density of at least $3+$), as this combination of features is characteristic of rupture-prone plaques.[1,2] Using these criteria, 30% of tissue sites (23/76) were classified as vulnerable plaques. (As the classification is based on the presence of a rupture-prone morphology rather than evidence of a rupture, the qualifier *suspected* vulnerable plaque is implied throughout the present work.)

In addition, 17% of spectral locations contained thrombotic plaques, i.e., plaques exhibiting a luminal thrombus (13/76). Of these, 46% were already diagnosed as vulnerable plaques using the above definition (6/13). The remaining 54%, not diagnosed as vulnerable plaques had adjacent vulnerable plaques that accounted for the presence of thrombus (7/13). A summary of the number of vulnerable plaque features found across all spectrally evaluated sites is given in Table 1. The breakdown among vulnerable plaques, thrombotic plaques, and stable lesions is overviewed in Fig. 3.
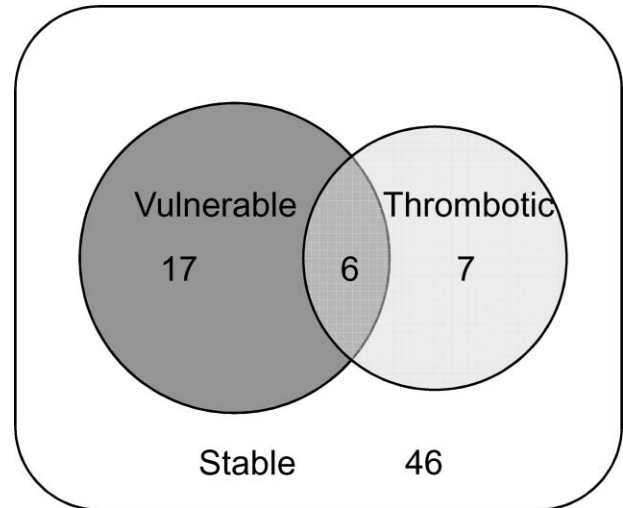

Fig. 3 The breakdown of vulnerable plaques, thrombotic plaques, and remaining lesions as assessed by histopathology. Note that some lesions can be both vulnerable and thrombotic.

3.2 Spectroscopic Parameters

Representative spectra and fits for DRS, IFS, and Raman modalities, collected from a carotid artery calcified atheromatous plaque, are displayed in Fig. 1. The excellent fits (small feature-less residuals) indicate that the spectral modeling is appropriate and adequately characterizes the experimental spectra.

In addition to the parameters derived directly from model fits ($c_{\beta-\text{car}}$, c_{ceroid}, and Raman thrombus), the following parameters were utilized in developing diagnostic algorithms for tissue characterization and vulnerable plaque detection. From IFS, two parameters were defined: C_E as the energy-normalized contribution of the collagen-like spectrum, and R_C as the relative amount of collagen, specified by:

$$C_E = \frac{C_{337}}{\langle \text{energy} \rangle}, \quad (3)$$

$$R_C = \frac{C_{337}}{C_{337} + E_{337}}, \quad (4)$$

with C_{337} being the collagen-like contribution, E_{337} the elastin/lipid-like contribution, and $\langle \text{energy} \rangle$ being the excitation energy (μJ/pulse) used to excite fluorescence. Lastly, a Raman parameter Σ was defined to characterize the lipid core:

$$\sum = \text{CC} + \text{FC/NC}, \quad (5)$$

with CC and FC/NC as the contributions of the cholesterol crystals and the foam cells/necrotic core constituent spectra, respectively.

3.3 Spectral Correlation with Plaque Morphology

Three spectral parameters, the DRS $c_{\beta-\text{car}}$ ($p < 0.002$), the DRS c_{ceroid} ($p < 0.02$), and the Raman Σ ($p < 0.1$), were shown to have a significant correlation with the histologically confirmed

presence of a large ($\geq 500\ \mu$m) NC or an accumulation ($\leq 65\ \mu$m deep, density $3+$) of SFCs, seen in 40 of 76 lesions. The diagnostic algorithm for detecting NC/SFCs using a decision threshold for the combination of the three mentioned spectral parameters, determined by logistic regression, had a sensitivity of 83% [68 to 91%] and a specificity of 75% [59 to 86%], where the numbers in brackets indicate 95% confidence intervals. The area under the ROC curve was 0.87 [0.79 to 0.95].

Each of two spectral parameters were shown to have a significant (p < 0.005) correlation with a histologically assessed thin ($\leq 65\ \mu$m) fibrous cap, seen in 22 out of the 76 lesions: the IFS R_C and IFS C_E. A diagnostic algorithm for detecting TFC using a decision threshold for these two spectral parameters determined by logistic regression had a sensitivity of 91% [72 to 98%] and a specificity of 62% [46 to 76%]. The area under the ROC curve was 0.85 [0.74 to 0.96]. For the purpose of developing the diagnostic algorithm only, the nonatherosclerotic intimal fibroplasia samples were excluded from the analysis, as they are not plaques and do not have a fibrous cap.

Seven spectral locations had a relatively large contribution ($\sim$10% of normalized Raman signal) from the thrombus constituent spectrum [Fig. 1(e)]. A diagnostic algorithm for detecting thrombotic plaques using a decision threshold for the Raman thrombus contribution determined by logistic regression achieved a sensitivity of 31% [13 to 58%] and a specificity of 97% [89 to 99%]. The area under the ROC curve was 0.66 [0.48 to 0.84]. Lastly, the Raman CM contribution also correlated with the presence of calcified plaques, achieving 88% accuracy in discriminating calcified plaques and noncalcified lesions.

3.4 *Spectral Diagnosis of Vulnerable Plaques*

The prior spectroscopic diagnostic algorithms were used in combination to classify plaques as vulnerable ($n = 23$), characterized by both a TFC and large NC/SFC, or nonvulnerable ($n = 53$) (see Fig. 3). The algorithm to classify these plaques used the two individual spectroscopic algorithms for detecting TFC and NC/SFC described before as decision stumps, requiring both to be positive for the combined algorithm to return positive for vulnerable plaque. All combinations of operating points on the ROC curve of each individual spectroscopic algorithm were used to generate the ROC curve for the combined algorithm for detecting vulnerable plaques. The area under the ROC curve for the combined algorithm, shown in Fig. 4, was 0.90 [0.81 to 0.99]. We selected the point on the ROC curve (indicated) that maximized test efficiency (overall accuracy) at 79%. This particular point achieved a sensitivity of 96% [79 to 99%], specificity of 72% [58 to 82%], PPV of 59% [44 to 74%], and NPV of 97% [87 to 99%]. The decision chart, including numbers of true positives (TP), true negatives (TN), false positives (FP), and false negatives (FN) for that particular operating point, is also shown in Fig. 4.

We also developed an algorithm for classifying vulnerable plaques that have not yet thrombosed plus thrombotic plaques ($n = 30$), which together represent plaques that may cause acute ischemic events (see Fig. 3). As mentioned earlier, 7/13 of these thrombotic plaques most probably resulted from an adjacent plaque rupture, as they did not exhibit vulnerable pathology at the spectral evaluation site itself (Fig. 3). The spectroscopic algorithm to detect this combined set of plaques used the three individual spectroscopic algorithms for detecting a TFC, NC/SFCs, and thrombus as decision stumps, requiring either TFC and NC/SFCs to be positive or for the thrombus algorithm to be positive. All combinations of operating points for the three individual spectroscopic algorithms were used to generate a single ROC curve for the algorithm for detecting the combined set of vulnerable or thrombotic plaques. The area under the resulting ROC curve, shown in Fig. 5, is 0.88 [0.80 to 0.96]. We selected the point on the ROC curve (indicated) that maximizes test efficiency at 80%. This particular point achieved a sensitivity of 93% [79 to 98%], specificity of 72% [58 to 83%], PPV of 68% [53 to 80%], and NPV of 94% [81 to 98%]. The decision chart, including numbers of TP, TN, FP, and FN for that particular operating point, is also shown in Fig. 5.

4 Discussion

Although the results and the upcoming discussion pertain to the *ex vivo* data, this study is the first to demonstrate the ability to collect MMS data *in vivo* from human patients in clinically acceptable times. This underscores the potential of multimodal spectroscopy techniques for future clinical applications. We also
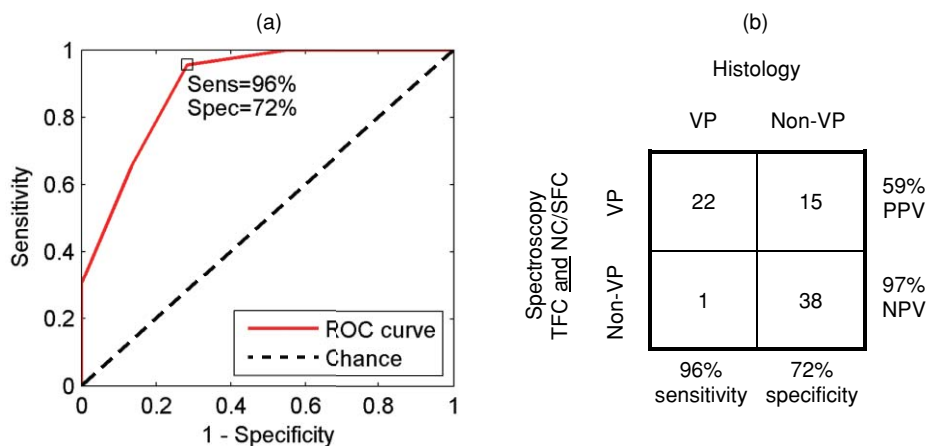

Fig. 4 ROC curve for the combined algorithm (a) for the detection of vulnerable plaques, and the decision chart (b) for the particular operating point indicated on the ROC that maximizes test efficiency. Area under the ROC curve = 0.90.
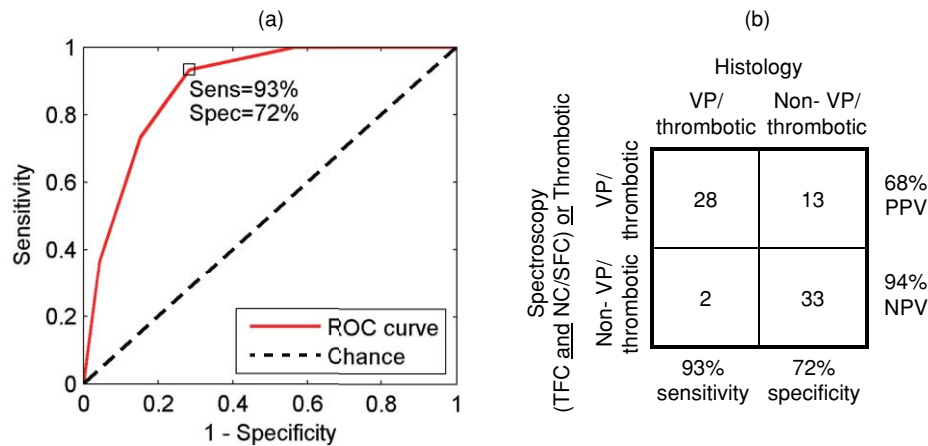
Fig. 5 ROC curve for the combined algorithm (a) for the detection of vulnerable or thrombotic plaques, and the decision chart (b) for the particular operating point indicated on the ROC. Area under the ROC curve = 0.88.

note that the development of the unitary MMS probe eliminated sampling error in data collection across spectral modalities at a particular tissue site, overcoming a limitation from previous studies.[13]

4.1 Spectral Correlation with Plaque Morphology

The quantitative spectroscopic information provided by MMS correlates with plaque morphology determined by histology. Moreover, there is sound physical basis and justification for the agreement between spectroscopy and histology rather than simply statistical correlations.

The algorithm for detecting NC /SFCs is consistent with previously published work, in which β-carotene from DRS was used to detect SFCs,[12] and the Raman Σ contribution[9,13,24] was used to detect lipid pools. However, this is the first time that such an algorithm is proposed that utilizes both DRS and Raman spectral parameters in a joint classification. Moreover, we note that the two contributions compensate for each other, with more accurate classification resulting if both the DRS and Raman parameters are used together than if either one is used alone. The misclassified samples are best explained by the discrete thresholds for defining a large NC ($\geq$500 μm) or an accumulation of SFCs (density 3 +), or the presence of NC too deep in tissue beyond the sampling volume of the probe. Many of these misclassifications are expected, since spectroscopy integrates the morphology-specific signals over its sampling volume, whereas our histological categorization is done using discrete thresholds.

Fluorescence has been used previously to detect the thickness of a plaque fibrous cap.[13,25] The diagnostic algorithm presented makes physical sense, as thicker fibrous cap samples had, on average, a larger contribution of collagen, indicated by the high values of both R_C and C_E. Conversely, TFC samples had lower values of those two IFS parameters. The chosen classification boundary exhibits a very high sensitivity at the expense of a low specificity. The false positive samples, the histologically thick fibrous caps that were misclassified spectroscopically as TFCs, are almost all explained by the presence of SFCs in the fibrous cap. An accumulation of SFCs can boost the elastin/lipid signal at the expense of the collagen-like signal to give an IFS signal

similar to that of a thin fibrous cap over a necrotic core. The remaining misclassifications can be explained by the presence of a variable size fibrous cap and the usage of discrete thresholds (65 μm) for histological classification.

Detection of thrombotic plaques using the Raman spectroscopic signature of pure thrombus has not, to our knowledge, been done before. We were able to extract a Raman spectrum from a pure thrombus and identify contributions of that spectrum to that of several thrombotic plaques. Moreover, features of the thrombus basis spectrum can be seen in the known Raman spectra of platelets,[26] fibrin,[27] and hemoglobin [Fig. 1(e)], the physical constituents of thrombus (data not shown). However, several other histologically thrombotic specimens did not contain a contribution from the thrombus basis spectrum; these are most likely explained by the relatively small physical size (average thickness ∼150 μm) of these thrombi.

4.2 Spectral Diagnosis of Vulnerable Plaques

We have demonstrated the ability to use the aforementioned individual diagnostic algorithms for TFC and large NC/SFC to detect vulnerable plaques with an excellent sensitivity and NPV. The one false negative vulnerable plaque is the result of not being able to detect its thin fibrous cap by the individual TFC algorithm. The 15 false positive vulnerable plaques are the result of the algorithm being aggressive in classifying borderline lesions as vulnerable plaques. Interestingly, six of these plaques contained intraplaque hemorrhage or thrombus from an adjacent ruptured vulnerable plaque. As a result, perhaps these sites are not really false positives but rather should have been histologically classified as vulnerable plaques in the first place. In detecting vulnerable plus thrombotic plaques, the combined algorithm for detecting TFC and large NC/SFCs or thrombus demonstrates that MMS can identify a potentially lethal pathology before it becomes clinically evident.

4.3 Comparison to Related Studies

The present study using MMS detected vulnerable plaques with sensitivity of 96% and specificity of 72% for the chosen point on the ROC curve. In previous work from our laboratory, Raman

spectroscopy alone detected vulnerable plaques with sensitivity of 79% and specificity of 85%.[9] A study from another group using near-infrared spectroscopy-detected features of vulnerable plaque (lipid pool, thin cap, and inflammatory cells) with sensitivity of 77 to 90% and specificity of 89 to 93%.[28] Similarly, studies with optical coherence tomography (OCT) reported the following sensitivities and specificities: 71 to 79% and 97 to 98% for detecting fibrous plaques, 95 to 96% and 97% for detecting fibrocalcific plaques, and 90 to 94% and 90 to 92% for lipid-rich plaques, respectively.[29] Note that the near-infrared and OCT studies did not attempt to explicitly detect vulnerable plaques, so perhaps a direct comparison to the present MMS study cannot be made. Also, the three comparative studies described did not describe the ROC for their classifiers. Nevertheless, the combination of sensitivity and specificity of the present MMS study is roughly in line with those other studies.

4.4 Limitations

There are several limitations to the present study. The first one is that the presented diagnostic results are completely based on the *ex vivo* dataset. Although we also demonstrated the ability to collect spectra *in vivo*, we did not attempt to draw any implications from the *in vivo* dataset for the reasons mentioned earlier. As a result, we are not claiming that any of the discussed results should necessarily hold *in vivo*. Second, the performance of the diagnostic algorithms was assessed on the same dataset on which the algorithms were developed. Although we appropriately used leave-one-out cross-validation to avoid overfitting, it would have been preferable to have another large set of data for prospective testing. Consequently, the presented algorithms and performance indications should be considered preliminary.

4.5 Future Work

OCT and near-infrared spectroscopy are fast techniques that can result in real-time images of the arterial wall—capabilities that MMS does not currently have. However, MMS is able to provide more detailed chemical and morphological information about the lesion constituents than OCT or near-infrared spectroscopy. Like these two techniques, MMS requires a saline flush to minimize the effects of blood/hemoglobin on the measurement. The ultimate goal for MMS is to combine it with a faster imaging technique like OCT. The faster imaging technique would provide detailed anatomical information of larger portions of the artery wall to identify more suspicious regions of interest. These regions of interest would then be further analyzed with MMS to provide additional chemical and morphological detail and evaluate plaque vulnerability.

In the next step of our research, we intend to perform a fully prospective study to further validate the stated results. In addition, we will begin development of an advanced instrument and probe that would enable side-viewing, catheter-driven, data collection in the presence of flowing blood, as we aim to bring MMS into the clinical arena.

5 Conclusion

We demonstrate the ability to detect several morphologic features of vulnerable atherosclerotic plaques, including a thin fibrous cap, a large necrotic core, and an accumulation of superficial foam cells, from *ex vivo* MMS spectra. To achieve this, several parameters from the individual MMS modalities are used, providing a physical basis for comparisons. Most importantly, we demonstrate the ability to detect vulnerable plaques with a sensitivity of 96%, specificity of 72%, and a negative predictive value of 97%. We also demonstrate the ability, for the first time, to detect a thrombus on the surface of a plaque using its Raman spectral signature, indicating a previous plaque rupture. Lastly, we demonstrate the feasibility of collecting *in vivo* MMS data in clinically acceptable times that could provide real-time feedback to the physician. These encouraging results indicate the potential for MMS to serve as a robust, catheter-based, clinical diagnostic technique. In the future, we hope to eventually develop MMS into an *in vivo* technique for the early identification of patients with suspected vulnerable plaques, affording an opportunity for therapeutic intervention before the occurrence of catastrophic plaque rupture.

References

1. R. Virmani, A. P. Burke, F. D. Kolodgie, and A. Farb, "Vulnerable plaque: the pathology of unstable coronary lesions," *J. Intervent. Cardiol.* **15**(6), 439–446 (2002).
2. R. Virmani, E. R. Ladich, A. P. Burke, and F. D. Kolodgie, "Histopathology of carotid atherosclerotic disease," *Neurosurg.* **59** (5 Suppl 3), S219–227; discussion S213–213 (2006).
3. M. Naghavi, P. Libby, E. Falk, S. W. Casscells, S. Litovsky, J. Rumberger, J. J. Badimon, C. Stefanadis, P. Moreno, G. Pasterkamp, Z. Fayad, P. H. Stone, S. Waxman, P. Raggi, M. Madjid, A. Zarrabi, A. Burke, C. Yuan, P. J. Fitzgerald, D. S. Siscovick, C. L. de Korte, M. Aikawa, K. E. Juhani Airaksinen, G. Assmann, C. R. Becker, J. H. Chesebro, A. Farb, Z. S. Galis, C. Jackson, I. K. Jang, W. Koenig, R. A. Lodder, K. March, J. Demirovic, M. Navab, S. G. Priori, M. D. Rekhter, R. Bahr, S. M. Grundy, R. Mehran, A. Colombo, E. Boerwinkle, C. Ballantyne, W. Insull, Jr., R. S. Schwartz, R. Vogel, P. W. Serruys, G. K. Hansson, D. P. Faxon, S. Kaul, H. Drexler, P. Greenland, J. E. Muller, R. Virmani, P. M. Ridker, D. P. Zipes, P. K. Shah, and J. T. Willerson, "From vulnerable plaque to vulnerable patient: a call for new definitions and risk assessment strategies: Part I," *Circulation* **108**(14), 1664–1672 (2003).
4. N. Takaya, C. Yuan, B. Chu, T. Saam, N. L. Polissar, G. P. Jarvik, C. Isaac, J. McDonough, C. Natiello, R. Small, M. S. Ferguson, and T. S. Hatsukami, "Presence of intraplaque hemorrhage stimulates progression of carotid atherosclerotic plaques: a high-resolution magnetic resonance imaging study," *Circulation* **111**(21), 2768–2775 (2005).
5. M. J. Kern and B. Meier, "Evaluation of the culprit plaque and the physiological significance of coronary atherosclerotic narrowings," *Circulation* **103**(25), 3142–3149 (2001).
6. L. Marcu, Q. Y. Fang, J. A. Jo, T. Papaioannou, A. Dorafshar, T. Reil, J. H. Qiao, J. D. Baker, J. A. Freischlag, and M. C. Fishbein, "*In vivo* detection of macrophages in a rabbit atherosclerotic model by time-resolved laser-induced fluorescence spectroscopy," *Atheroscler.* **181**(2), 295–303 (2005).
7. F. A. Jaffer, C. Vinegoni, M. C. John, E. Aikawa, H. K. Gold, A. V. Finn, V. Ntziachristos, P. Libby, and R. Weissleder, "Real-time catheter molecular sensing of inflammation in proteolytically active atherosclerosis," *Circulation* **118**(18), 1802–1809 (2008).
8. P. R. Moreno and J. E. Muller, "Detection of high-risk atherosclerotic coronary plaques by intravascular spectroscopy," *J. Intervent. Cardiol.* **16**(3), 243–252 (2003).

9. J. T. Motz, M. Fitzmaurice, A. Miller, S. J. Gandhi, A. S. Haka, L. H. Galindo, R. R. Dasari, J. R. Kramer, and M. S. Feld, "*In vivo* Raman spectral pathology of human atherosclerosis and vulnerable plaque," *J. Biomed. Opt.* **11**(2), 021003 (2006).

10. J. T. Motz, M. Hunter, L. H. Galindo, J. A. Gardecki, J. R. Kramer, R. R. Dasari, and M. S. Feld, "Optical fiber probe for biomedical Raman spectroscopy," *Appl. Opt.* **43**(3), 542–554 (2004).

11. J. T. Motz, S. J. Gandhi, O. R. Scepanovic, A. S. Haka, J. R. Kramer, R. R. Dasari, and M. S. Feld, "Real-Time Raman System for *In Vivo* Disease Diagnosis," *J. Biomed. Opt.* **10**(3), 031113 (2005).

12. G. O. Angheloiu, J. T. Arendt, M. G. Muller, A. S. Haka, I. Georgakoudi, J. T. Motz, O. R. Scepanovic, B. D. Kuban, J. Myles, F. Miller, E. A. Podrez, M. Fitzmaurice, J. R. Kramer, and M. S. Feld, "Intrinsic fluorescence and diffuse reflectance spectroscopy identify superficial foam cells in coronary plaques prone to erosion," *Arterioscler., Thromb., Vascular Biol.* **26**(7), 1594–1600 (2006).

13. O. R. Scepanovic, M. Fitzmaurice, J. A. Gardecki, G. O. Angheloiu, S. Awasthi, J. T. Motz, J. R. Kramer, R. R. Dasari, and M. S. Feld, "Detection of morphological markers of vulnerable atherosclerotic plaque using multimodal spectroscopy," *J. Biomed. Opt.* **11**(2), 021007 (2006).

14. O. R. Scepanovic, Z. Volynskaya, C. R. Kong, L. H. Galindo, R. R. Dasari, and M. S. Feld, "A multimodal spectroscopy system for real-time disease diagnosis," *Rev. Scient. Instrum.* **80**(4), 043103 (2009).

15. T. J. Farrell, M. S. Patterson, and B. Wilson, "A diffusion-theory model of spatially resolved, steady-state diffuse reflectance for the noninvasive determination of tissue optical-properties *in vivo*," *Med. Phys.* **19**(4), 879–888 (1992).

16. J. R. Mourant, T. Fuselier, J. Boyer, T. M. Johnson, and I. J. Bigio, "Predictions and measurements of scattering and absorption over broad wavelength ranges in tissue phantoms," *Appl. Opt.* **36**(4), 949–957 (1997).

17. J. M. Schmitt and G. Kumar, "Optical scattering properties of soft tissue: A discrete particle model," *Appl. Opt.* **37**(13), 2788–2797 (1998).

18. V. N. Karnaukhov, T. B. Tataryunas, and V. V. Petrunyaka, "Accumulation of carotenoids in brain and heart of animals on aging; the role of carotenoids in lipofuscin formation," *Mechan. Age. Develop.* **2**, 201–210 (1972).

19. R. L. P. van Veen, W. Verkruysse, and H. J. C. M. Sterenborg, "Diffuse-reflectance spectroscopy from 500 to 1060 nm by correction for inhomogeneously distributed absorbers," *Opt. Lett.* **27**(4), 246–248 (2002).

20. Q. G. Zhang, M. G. Muller, J. Wu, and M. S. Feld, "Turbidity-free fluorescence spectroscopy of biological tissue," *Opt. Lett.* **25**(19), 1451–1453 (2000).

21. H. P. Buschman, G. Deinum, J. T. Motz, M. Fitzmaurice, J. R. Kramer, A. Van Der Laarse, A. V. Bruschke, and M. S. Feld, "Raman microspectroscopy of human coronary atherosclerosis: Biochemical assessment of cellular and extracellular morphologic structures *in situ*," *Cardiovasc. Pathol.* **10**(2), 69–82 (2001).

22. See http://ihtsdo.org.

23. R. O. Duda, P. E. Hart, and D. G. Stork, *Pattern Classification*, Wiley, New York (2001).

24. H. P. Buschman, J. T. Motz, G. Deinum, T. J. Romer, M. Fitzmaurice, J. R. Kramer, A. Van Der Laarse, A. V. Bruschke, and M. S. Feld, "Diagnosis of human coronary atherosclerosis by morphology-based Raman spectroscopy," *Cardiovasc. Pathol.* **10**(2), 59–68 (2001).

25. K. Arakawa, K. Isoda, T. Ito, K. Nakajima, T. Shibuya, and F. Ohsuzu, "Fluorescence analysis of biochemical constituents identifies atherosclerotic plaque with a thin fibrous cap," *Arterioscler., Thromb., Vascular Biol.* **22**(6), 1002–1007 (2002).

26. D. Aslanian, H. Vainer, and J. P. Guesdon, "Thermotropic state transition in isolated platelet membranes studied by Raman spectroscopy," *Eur. J. Biochem.* **131**(3), 555–558 (1983).

27. M. Jelinek, R. Cristescu, T. Kocourek, V. Vorlicek, J. Remsa, L. Stamatin, D. Mihaiescu, I. Stamatin, I. N. Mihailescu, and D. B. Chrisey, "Thin films growth in MAPLE; application to fibrinogen," *J. Phys.: Conf. Series* **59**, 22–27 (2007).

28. P. R. Moreno, R. A. Lodder, K. R. Purushothaman, W. E. Charash, W. N. O'Connor, and J. E. Muller, "Detection of lipid pool, thin fibrous cap, and inflammatory cells in human aortic atherosclerotic plaques by near-infrared spectroscopy," *Circulation* **105**(8), 923–927 (2002).

29. H. Yabushita, B. E. Bouma, S. L. Houser, H. T. Aretz, I. K. Jang, K. H. Schlendorf, C. R. Kauffman, M. Shishkov, D. H. Kang, E. F. Halpern, and G. J. Tearney, "Characterization of human atherosclerosis by optical coherence tomography," *Circulation* **106**(13), 1640–1645 (2002).